



Water calibration measurements for neutron radiography: Application to water content quantification in porous media[☆]

M. Kang^{a,b,*}, H.Z. Bilheux^{b,**}, S. Voisin^c, C.L. Cheng^a, E. Perfect^a, J. Horita^d, J.M. Warren^e

^a Department of Earth and Planetary Sciences, University of Tennessee, Knoxville, TN, USA

^b Chemical and Engineering Materials Division, Oak Ridge National Laboratory, Oak Ridge, TN, USA

^c Computational Sciences and Engineering Division, Oak Ridge National Laboratory, Oak Ridge, TN, USA

^d Department of Geosciences, Texas Tech University, Lubbock, TX, USA

^e Environmental Sciences Division, Oak Ridge National Laboratory, Oak Ridge, TN, USA

ARTICLE INFO

Article history:

Received 19 April 2012

Received in revised form

20 December 2012

Accepted 21 December 2012

Available online 9 January 2013

Keywords:

Neutron radiography

Water calibration

Quantification

Porous media

ABSTRACT

Using neutron radiography, the measurement of water thickness was performed using aluminum (Al) water calibration cells at the High Flux Isotope Reactor (HFIR) Cold-Guide (CG) 1D neutron imaging facility at Oak Ridge National Laboratory, Oak Ridge, TN, USA. Calibration of water thickness is an important step to accurately measure water contents in samples of interest. Neutron attenuation by water does not vary linearly with thickness mainly due to beam hardening and scattering effects. Transmission measurements for known water thicknesses in water calibration cells allow proper correction of the underestimation of water content due to these effects.

As anticipated, strong scattering effects were observed for water thicknesses greater than 0.2 cm when the water calibration cells were positioned close to the face of the detector/scintillator (0 and 2.4 cm away, respectively). The water calibration cells were also positioned 24 cm away from the detector face. These measurements resulted in less scattering and this position (designated as the sample position) was used for the subsequent experimental determination of the neutron attenuation coefficient for water.

Neutron radiographic images of moist Flint sand in rectangular and cylindrical containers acquired at the sample position were used to demonstrate the applicability of the water calibration. Cumulative changes in the water volumes within the sand columns during monotonic drainage determined by neutron radiography were compared with those recorded by direct reading from a burette connected to a hanging water column. In general, the neutron radiography data showed very good agreement with those obtained volumetrically using the hanging water-column method. These results allow extension of the calibration equation to the quantification of unknown water contents within other samples of porous media.

© 2013 Elsevier B.V. All rights reserved.

1. Introduction

Neutron imaging is a complementary technique to X-ray imaging and is used in many applications in various fields such as materials science, physics, biology, geology, and archeology

[☆]This manuscript has been authored by UT-Battelle, LLC, under Contract No. DE-AC05-00OR22725 with the U.S. Department of Energy. The United States Government retains and the publisher, by accepting the article for publication, acknowledges that the United States Government retains a non-exclusive, paid-up, irrevocable, world-wide license to publish or reproduce the published form of this manuscript, or allow others to do so, for United States Government purposes.

* Corresponding author at: Department of Earth and Planetary Sciences, University of Tennessee, 1412 Circle Dr, Knoxville, TN 37996-1410, USA.

** Corresponding author.

E-mail addresses: kangm@ornl.gov (M. Kang), bilheuxhn@ornl.gov (H.Z. Bilheux).

[1,2]. Neutrons interact with atomic nuclei and this interaction does not show periodic regularity with the atomic number. Neutrons are particularly sensitive to light elements such as hydrogen (H), lithium (Li), and boron (B), while being relatively insensitive to metals such as Al [1,2]. Thus, neutrons are well suited for the investigation of water movement in natural and engineered porous media. X-rays and magnetic resonance imaging (MRI) have also been used in the past to study water in porous media [3–6]. X-ray imaging uses tracers to enhance contrast since X-rays are not as sensitive to light elements, such as H, as neutrons [4]. The quantitative study of water in porous media using MRI is limited by the range of pore sizes that can be imaged and the presence of paramagnetic elements in the sample [6]. Quantitative measurements of water thickness using neutron imaging have been used in a variety of research areas, such as fuel cells [7,8], plant roots [9,10], and rocks and soils

[11–15]. Transmission of a polychromatic neutron beam through a heterogeneous sample is given by

$$I = \int I_0(E) \exp \left[-\sum_{i=1}^n (\tau_i \Sigma_i(E)) \right] dE \quad (1)$$

where I and I_0 are the transmitted and incident beam intensity, respectively, τ_i is the thickness of each element i , and $\Sigma_i(E) = [(\sigma_i(E)m\rho N_A)/(M)]$, where $\sigma_i(E)$ is the total cross-section of an element (barns), m is the number of moles of an element in a molecule, ρ is the density (g/cm^3), N_A is Avogadro's number ($6.022 \times 10^{23} \text{ mol}^{-1}$), and M is the molecular weight (g/mol) of the sample over the range of the effective neutron energy spectrum.

Experimental determination of water thickness in a sample requires careful measurement of the attenuation coefficient of the sample container (if any) and other parts of the sample that do not contain water. The effects of the container and other materials can be experimentally removed by dividing the image of the sample containing water (called the 'wet' sample in this publication) by the image of the dry sample in the same container (called the 'dry' sample in this publication)

$$I_w/I_d = \int \exp [-\tau_w \Sigma_w(E)] dE \quad (2)$$

where I_w is the transmitted intensity of the 'wet' sample, I_d is the transmitted intensity of the 'dry' sample, τ_w is the water thickness, and $\Sigma_w(E)$ is the attenuation coefficient of water. In polychromatic beam measurements, only the average value of $\Sigma_w(E)$ can be obtained rather than its value at different wavelengths. Wavelength-discrete $\Sigma_w(E)$ values can be achieved by neutron monochromatization using a double-crystal monochromator device [16] or a velocity selector/chopper system [17,18] for continuous sources.

For neutron imaging, considerable effort must be made to achieve a parallel and uniform beam, with limited background scattering sources, using variable collimators providing balance between the neutron flux and image resolution. The spatial resolution achieved can be quantified in terms of the geometric unsharpness (U_g):

$$U_g = l/(L/D) \quad (3)$$

where l is the distance between the sample and the detector, D is the aperture diameter, and L is the distance between the aperture and the detector. The geometric unsharpness increases as the sample-to-detector distance increases and as the L/D ratio decreases.

Optimization of the sample position in relation to the detector (scintillator) position has proven to be critical for water thickness measurements of samples [19–21]. The relationship between the attenuated beam intensity and water thickness is not linear and this non-linearity increases as the water content of the sample increases and/or as the distance between sample and detector decreases, resulting in the underestimation of water content in thick samples with high water contents. Lehmann et al. [19] observed deviations from the exponential law, Eq. (2), for water thicknesses greater than 0.2 cm even at a 15 cm sample to detector distance. The non-linearity is due to beam hardening and neutron scattering effects. Beam hardening occurs if the neutron beam is polychromatic; low energy neutrons are more attenuated than high energy neutrons, which results in variations in the measured attenuation. The scattering effects can be more problematic for water because the attenuation occurs due to incoherent scattering. The scattered neutrons can reach the detector and result in the increase of the transmission, which leads to a less water content estimation in the sample.

Different approaches have been proposed to quantify water content in samples using polychromatic neutron imaging. One is

to restrict measurements to sections of the sample with a total water thickness less than 0.1 or 0.2 cm [22,23] in order to minimize beam hardening and scattering effects. Another approach is to correct these effects using the point scattered functions based on Monte Carlo simulations after considering the sample and the experimental set-up (i.e. energy spectrum, detector type, distance between sample and detector) [20]. The latter correction does not provide a universal solution as it relies on a specific experimental set-up [24]. As an alternative, an empirical water thickness calibration equation can be developed for a specific instrumentation configuration [12,25].

The specific objectives of this research were to: (1) investigate scattering effects at different calibration sample locations (i.e. varying distance between the sample and detector); (2) obtain water attenuation coefficients for the High Flux Isotope Reactor (HFIR) Cold Guide (CG) 1D neutron imaging facility using water calibration cells positioned at the optimal sample location for a sample with high water content; and (3) apply this calibration equation to quantify water content within a partially-saturated porous medium and compare the results with conventional hanging water column experiments.

2. Methodology

2.1. The HFIR CG-1D neutron prototype imaging instrument

Neutron radiography of water calibration cells and Flint sand were performed at the HFIR CG-1D neutron imaging facility at the Oak Ridge National Laboratory (ORNL). For polychromatic neutron imaging, apertures with variable diameter sizes (pinhole geometry) can be used at the entrance of the He-filled flight path with a maximum L of 5.5 m. For this experiment, D and L are equal to 8 mm and 5 m respectively, resulting in a L/D of 625. A higher L/D ratio, i.e. smaller apertures and longer aperture to detector distances, reduces blur in an image and limits background scattering sources. The spectrum measured using a micro-channel plate (MCP) detector [26] with a flight path of approximately 5.5 m is shown in Fig. 1. The facility provides most neutrons between approximately 0.8 and 6 Å (with a peak at ~ 2.6 Å) [27]. The detector set-up is equipped with a 25 μm thick LiF/ZnS scintillator and DW936 IkonL ANDOR™ charge coupled device (CCD) camera system. In order to reduce dark current, the CCD camera is equipped with a Peltier cooling system and is routinely cooled down to -60°C . For these measurements, the neutron flux is $5 \times 10^5 \text{ cm}^{-2} \text{ s}^{-1}$, the field of view is approximately $7 \text{ cm} \times 7 \text{ cm}$, and the full width at half maximum (FWHM) at 24 cm is 212 μm . As indicated in Eq. (2), the attenuation of neutrons by water is

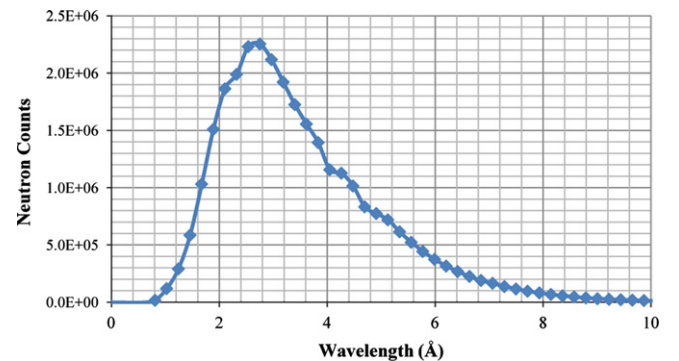


Fig. 1. CG-1D spectrum measured with an MCP detector at a flight path distance of approximately 5.5 m, with the chopper running at a frequency 40 Hz.

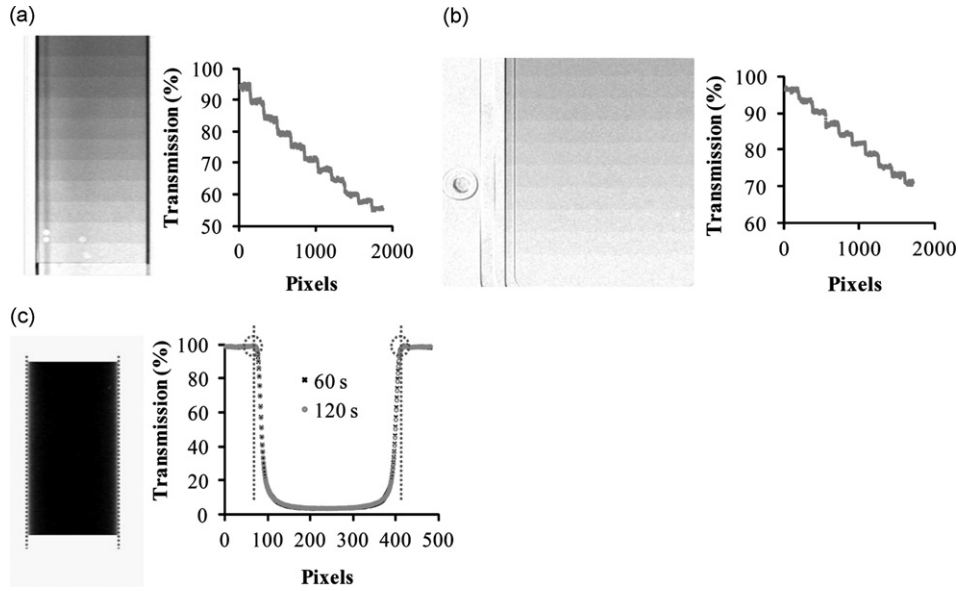


Fig. 2. Examples of wet transmission images for each calibration cell type after division by the dry cell and their corresponding transmission profiles. (a) rectangular calibration cell #1 with 11 steps of water thickness from 0.005 to 0.105cm (0.01 cm increment) with 600 s exposure time, (b) rectangular calibration cell #2 with 10 steps of water thickness from 0.005 to 0.050cm (0.005 cm increment) with 300(s exposure time, and (c) cylindrical calibration cell with water thickness ranging from 0–0.909cm with 120s exposure time (note: the transmission profile for the cell also includes results for 60s exposure time). All examples are for the 24 cm sample position.

neutron-energy dependent. Reported attenuation coefficients for ≤ 0.2 cm thick water layers are 6.45 cm^{-1} for cold neutrons and 3.38 cm^{-1} for thermal neutrons [28]. Since cold neutrons are more sensitive to the H atoms in water than thermal neutrons, the neutron sensitivity is greater for thinner water thicknesses at the HFIR CG-1D beamline.

2.2. Calibration cells

One cylindrical and two different rectangular aluminum (Al) calibration cell types (#1 and #2) were used to obtain water attenuation coefficients at the HFIR CG-1D. The engineering accuracy of the calibration cells was ± 0.01 mm. All of the cells were cleaned with detergent and rinsed with deionized water before use.

The #1 rectangular type cell had a cross-section of $1.9 \text{ cm} \times 10.5 \text{ cm}$, with a 0.01 cm thickness step increment. Radiographic images of the wet (i.e. filled with deionized water) and dry (i.e. no water) cell were measured using for water thickness ranging from 0.005 to 0.205 cm, 0.2–0.6 cm, 0.6–1 cm at two different sample positions 2.4 and 24 cm away from the detector with 600 s exposure time.

For replication, another series of measurements was performed with a #2 rectangular cell type. The dimensions of the cell were $6 \text{ cm} \times 4.2 \text{ cm}$, with incremental thickness steps of 0.005 cm for less than 0.15 cm water thickness measurement, and incremental thickness steps of 0.01 cm for above 0.15 cm water thickness measurement. The wet and dry cells were imaged for the 0.005–0.05 cm, 0.105–0.15 cm, 0.2–0.3 cm, and 0.41–0.5 cm water thickness ranges. All of these measurements were made at two different sample positions: against the detector (0 cm) and 24 cm away from the detector with 300 s exposure time.

The cylindrical water calibration cell with an inner diameter of 0.909 cm was also imaged at a distance of 24 cm from the detector with 60 s and 120 s exposure time. For the cylindrical cell geometry, the known water thickness of the cell is equivalent

to the chord length of a circle (C_{ij})

$$C_{ij} = 2\sqrt{r^2 - a_{(i,j)}^2} \quad (4)$$

where r is the radius of the cylindrical cell (cm) and $a_{(i,j)}$ is the distance from the center of the cell to the pixel (i,j) (cm). Since most neutron radiographic images of our porous media samples were acquired using a cylindrical Al chamber, any effects on the attenuation and scattering of neutrons due to the geometry of the sample are of particular interest.

2.3. Image analysis

All image processing and quantitative analyses were performed using the MATLAB (Version 7.11, R2010b-SP1, Math Works, Inc., 2011) [29] and ImageJ (Version 1.43 m, National Institutes of Health, 2009) [30] software packages. The measured transmitted neutron intensity in the sample depends on the incident neutron beam intensity and the detector efficiency at detecting and converting neutrons. Each pixel value of the image ranged from ~ 900 (CCD default offset) to 65,535 according to the transmitted neutron intensity. Background scattering coming from the beamline equipment has been measured to be less than 1% and thus can be ignored during the image processing. Images of the water calibration cells were analyzed by the following procedures.

First, the collected raw images of the wet and dry calibration cells were normalized (to correct for background noises, inhomogeneities of beam and detector, and fluctuations of neutron flux) with respect to reference images of the open beam and dark field using the following expression:

$$I_{\text{wet}} = f_r \frac{I_{(\text{Wet Sample Image})} - I_{(\text{Dark Field})}}{I_{(\text{Open Beam})} - I_{(\text{Dark Field})}},$$

$$I_{\text{dry}} = f_r \frac{I_{(\text{Dry Sample Image})} - I_{(\text{Dark Field})}}{I_{(\text{Open Beam})} - I_{(\text{Dark Field})}} \quad (5)$$

where f_r is the rescale factor to correct the neutron beam fluctuations and is based on the differences in the mean intensity values between the selected open beam area (i.e. no object) in the

sample images and the mean of the same area in the open beam images. The normalized images, I_{wet} and I_{dry} , were despeckled using a median filter (5 pixels \times 5 pixels) to remove bright pixels mainly due to scattered γ -rays. The normalized wet images (I_{wet}) were then divided by the normalized dry images (I_{dry}). Examples of the resulting images and their intensity profiles are shown in Fig. 2. The longer exposure time provides a higher neutron flux, resulting in less variation in the data and better resolution of the image. However, the different exposure times did not cause any differences in measuring the water thickness. The plot profiles for the cylindrical cell (Fig. 2c) with different exposure times are very similar. We selected a region of interest (ROI) for each water thickness from these images while adjusting to exclude any trapped air bubbles and computed the average transmission values of the selected ROIs. The average transmission values were then plotted according to the known water thickness steps for each calibration cell.

2.4. Porous medium and hanging water column set-up

Flint sand (Flint #13, U.S. Silica Company, Berkeley Springs, WV) was used as a model porous medium because it is mainly composed of quartz (99.8%) with grain diameters ranging from 0.11 mm to 0.60 mm, and a median grain diameter of 0.56 mm. Flint sand was passed through a 2 mm sieve, washed with distilled water to remove any soluble contaminants, and oven-dried before use. The quantification of water content by neutron imaging of this sand column was thus minimally affected by other water-containing materials such as organic matter or clay minerals. To set up a hanging water column an outlet at the base of the Al container was connected via Tygon tubing to a burette filled with distilled water as illustrated in Fig. 3a. Two kinds of Al sample containers were used for the study; a rectangular (2.40 cm width \times 2.62 cm thickness \times 6.35 cm height) and a cylindrical container with an inner diameter 2.56 cm and a height of 10 cm. The bottom of the Al container was covered with several layers of moist Whatman #4 filter paper after removing any air bubbles in the hanging water column by suction. The oven-dried sand was then incrementally moist-packed into the Al container to minimize particle segregation and air entrapment. The heights of the packed columns were \sim 5 cm to fit the entire porous medium within the field of view of the HFIR CG-1D. The sand columns were fully-saturated overnight prior to each experiment. At the facility, the top of the Al container was attached to the sample holder while allowing air to flow into the Al container through small holes. The sand columns were drained under quasi-equilibrium conditions by adjusting the height of the hanging water column to give various basal suction values, as illustrated

schematically in Fig. 3b. A photograph of the experimental set up is shown in Fig. 4.

Multiple radiographic images were acquired at each quasi-equilibrium state during the main drainage process with an exposure time of 60 s. The water level in the burette was recorded simultaneously and later used to compare the measurements of total water volumes determined by the neutron radiography and hanging water column methods.

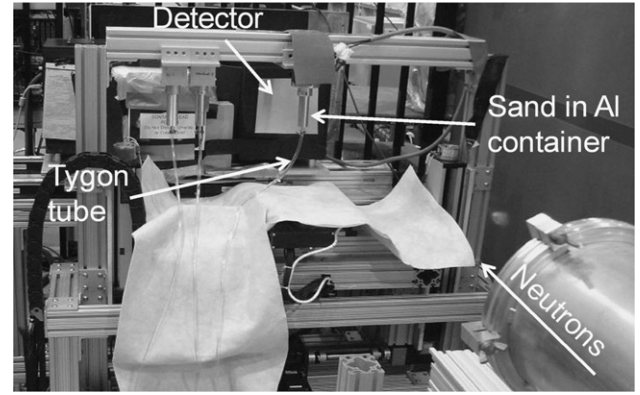


Fig. 4. Hanging water column set-up at HFIR CG-1D neutron imaging facility.

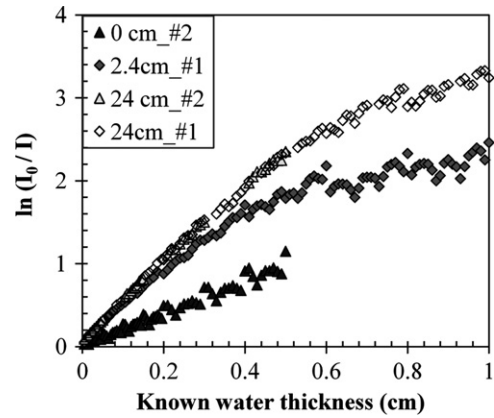


Fig. 5. Comparison of $\ln(I_0/I)$ values for rectangular water calibration cells (#1 and #2) at three different positions (0, 2.4, and 24 cm) from detector at the HFIR CG-1D neutron imaging facility. Note that images for cell #2 at 0 and 24 cm were normalized with respect to the open beam rather than the dry cell. The aluminum thickness for cell #2 was thinner than that for cell #1, and that normalization relative to the open beam was sufficient for cell #2 but not for cell #1 which required normalization by the dry image. Error bars (95% confidence intervals) for all the data are smaller than the symbols (error $\leq \pm 0.0064$ cm).

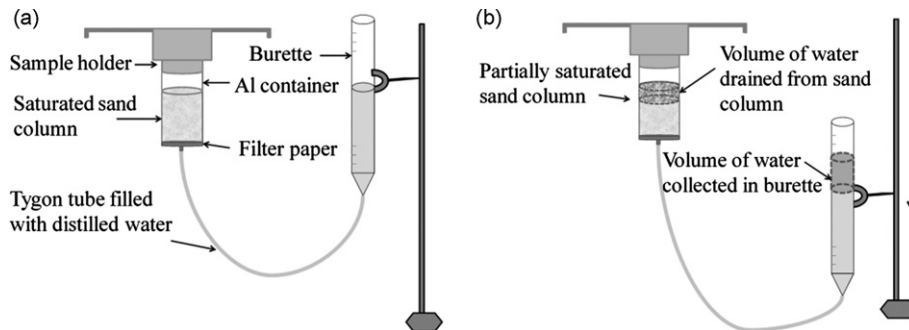


Fig. 3. Schematic diagram of the hanging water column setup: (a) initially saturated sand column and (b) drainage process achieved by lowering the burette. Note that the volume of water drained from the sand column is equal to the volume of water collected in the burette.

3. Results and discussion

3.1. Effect of sample to detector distance

Fig. 5 illustrates that the transmission values when the water calibration cells were placed close to the detector (0 cm or 2.4 cm) were more scattered along the exponentially declining trend line than the corresponding values for the water calibration cell placed 24 cm away from the detector. As expected, the shorter the distance between sample and detector, the higher the transmission values. The differences in the transmission values at the different sample positions became larger as the water thickness increased, mainly due to beam hardening and scattering effects [19–21], which increase with water thickness and decreasing distance to the detector.

Placing samples with high water contents against the detector creates severe and directional scattering that cannot be corrected for during image processing, as referenced in the literature [19–21]. However, for the HFIR CG-1D, when samples were positioned 24 cm away from the face of the detector, water thickness could be quantified since scattering effects became an offset that could be managed during image processing and analysis.

3.2. Determination of attenuation coefficients

Because the distance between the sample and detector influences the recorded transmission values of neutrons through the sample, attenuation coefficients were determined at the same location (24 cm from the detector) for the calibration cells and porous media images. We chose this location specifically for thick water samples to minimize the scattering effect at the sacrifice of image resolution. Kim et al. [23] estimated the effect of sample scattering on image formation of the sample by assuming that there is an infinite line charge of neutron scattering from water with a square cross-section.

$$I_S/I_T = (e^{-\Sigma\tau} - 1)\tau/(2\pi d) \quad (6)$$

where I_S is scattering intensity, I_T is transmitted intensity, Σ is the attenuation coefficient, τ is water thickness, and d is the sample to detector distance.

The net result of increasing the distance between the sample and the detector is a balance between increased unsharpness and decreased scattering. As shown in Fig. 6 increasing the sample-to-image detector distance results in decrease in scattering. To compare the unsharpness at different sample to detector distances a Gd straight edge from the Paul Scherrer Institute resolution mask was placed at 5 cm and 24 cm from the detector.

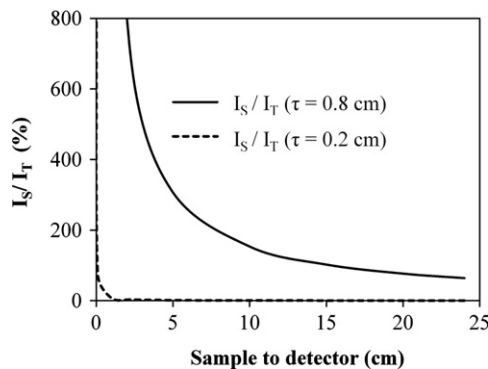


Fig. 6. The ratio of scattering intensity to the transmitted intensity as a function of sample to detector distance is predicted assuming $\Sigma = 6 \text{ cm}^{-1}$ using Eq. (6).

The edge spread function (ESF) was derived by vertical averaging along the edge of the straight Gd line image. The line spread function (LSF) was obtained by taking the numerical derivative of the ESF and the full width at half maximum (FWHM) of each of the LSF's was determined. The ESF's and LSF's for both locations are shown in Fig. 7. The FWHM values at 5 cm and 24 cm were 131 μm and 212 μm , respectively. Moving the sample from 24 cm to 5 cm from the detector resulted in $\sim 38\%$ decrease in measured unsharpness and $\sim 380\%$ increase in predicted scattering. Even though the unsharpness decreased as the sample to detector distance decreased, the percentage decrease was an order of magnitude less than the percentage increase due to scattering. For our thick water-rich samples we opted to reduce scattering effects at the expense of image resolution. For thinner, less water-rich samples, a smaller object to detector distance could be chosen to decrease unsharpness.

The data from each calibration cell showed little variation due to neutron beam fluctuations, different acquisition times, and other variables caused by neighboring beam lines or natural and fluorescent lights during data acquisition. To minimize statistical variations, data from all three calibration cells were pooled. Data for the cylindrical cells were restricted to chord lengths $> 1.5 \text{ mm}$ to eliminate edge effects.

To determine the attenuation coefficient for water at the HFIR CG-1D, calibration data from known water thickness were fitted to the transmission data for two different ranges of water calibration data sets ($\leq 0.2 \text{ cm}$ and $\leq 1 \text{ cm}$), using SAS 9.2 non-linear regression method [31]. The predicted water thickness values using the simple Beer–Lambert law with only one attenuation coefficient without any correction factor ($\Sigma = 5.30 \text{ cm}^{-1}$ for $\leq 0.2 \text{ cm}$ or 4.77 cm^{-1} for $\leq 1 \text{ cm}$ water calibration data set) show significant deviations from the known water thickness values as the water thickness increased (Fig. 8). Both attenuation coefficients significantly underestimated the known values beyond 0.5 cm of water thickness and the deviation was larger for the $\leq 0.2 \text{ cm}$ calibration data set selected to obtain the water attenuation coefficient than for the $\leq 1 \text{ cm}$ water data set. The deviation occurs when a polychromatic beam passing through a section of water preferentially loses the lower-energy parts of its spectrum, which results in underestimation of water thickness. In addition, the deviation is increased due to strong incoherent scattering of water depending on the water thickness.

In order to empirically correct for beam hardening and scattering effects, a correction parameter β was introduced to fit the calibration data by assuming $\Sigma_w = \Sigma + \beta\tau$ [15,25]:

$$\ln\left(\frac{I_{\text{dry}}}{I_{\text{wet}}}\right)_{(i,j)} = \Sigma\tau_{(i,j)} + \beta\tau_{(i,j)}^2 \quad (7)$$

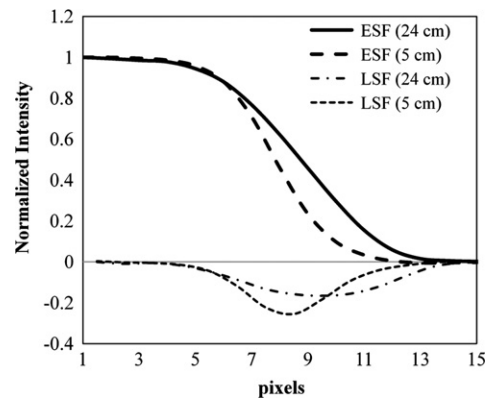


Fig. 7. Measured ESF's and LSF's for a Gd straight edge from the Paul Scherrer Institute resolution mask at 5 cm and 24 cm sample to detector distances.

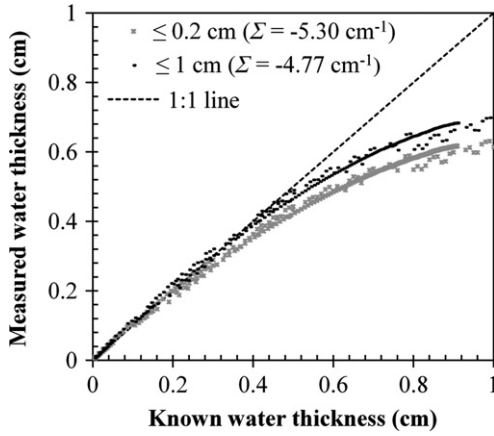


Fig. 8. Deviation of measured water thickness from the known water thickness when using attenuation coefficients obtained from the Beer–Lambert law for two different selected data ranges: ≤ 0.2 and ≤ 1 cm of water thickness.

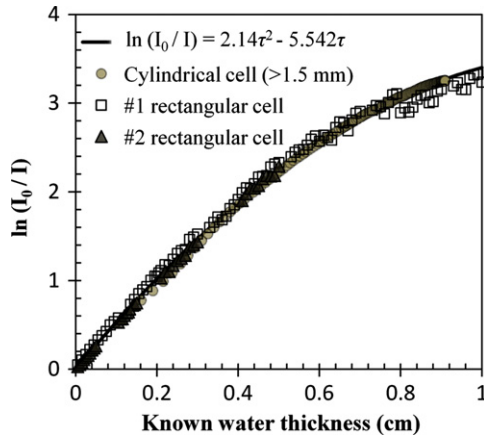


Fig. 9. Best fit of Eq. (7) to the measured neutron data versus known water thickness (τ) for all three calibration cell types located 24 cm away from the detector.

where I_{wet} and I_{dry} are the normalized wet and dry images, respectively. $\tau_{(i,j)}$ is the water thickness, and Σ_w is the attenuation coefficient of water.

The attenuation coefficient Σ and correction coefficient β were obtained by fitting Eq. (7) in SAS 9.2 using the Marquardt non-linear regression method [31] to neutron data up to 10 mm of water thickness. The fitted curve for all of the transmission data measured at HFIR CG-1D (including all three calibration cell types) shows a very good fit to the water calibration data (Fig. 9).

The estimated Σ and β values were implemented in MATLAB code to calculate the water thickness of the sample and applied to the cylindrical and rectangular water calibration cells and sand column images for validation of the calibration method. The water thickness of each pixel in the neutron radiographs of the rectangular and cylindrical water calibration cells was calculated using the following expression derived by solving Eq. (7) for $\tau_{(i,j)}$:

$$\tau_{(i,j)} = -\frac{\Sigma}{2\beta} - \sqrt{\left(\frac{\Sigma}{2\beta}\right)^2 - \frac{1}{\beta} \ln\left(\frac{I_{wet}}{I_{dry}}\right)_{(i,j)}} \quad (8)$$

where $\tau_{(i,j)}$ is water thickness in cm, $\Sigma = 5.542 \text{ cm}^{-1}$, $\beta = -2.140 \text{ cm}^{-2}$, and I_{wet} and I_{dry} are the normalized wet and dry images, respectively.

The water thicknesses of all the calibration data were predicted by transmission images using Eq. (8) (number of observations=289, root mean square error (RMSE)=0.2184, $R^2=0.9942$) with an

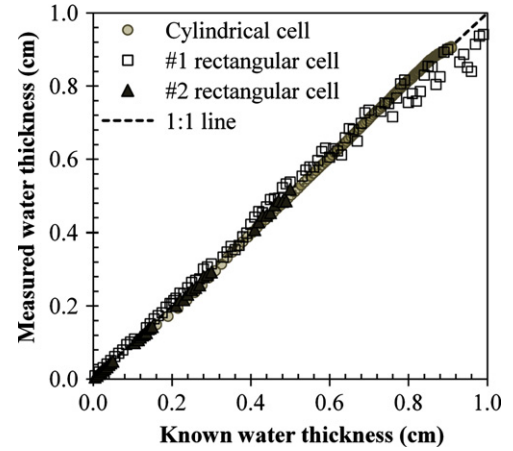


Fig. 10. Comparison of the measured average water thickness values using attenuation coefficients determined from calibration cell data and known water thickness values for the cylindrical and rectangular water calibration cells.

accuracy of ± 0.022 cm. The measured water thickness values from the neutron radiography were compared with those of the known water thickness from the water calibration cells (Fig. 10). The measured water thickness values for both the cylindrical and rectangular cells were close to the known water thickness values (from the engineering design) in the range between 0.15 cm and 0.8 cm. The results from the rectangular cells show some deviations from the 1 to 1 line at high water thicknesses (> 0.8 cm) possibly because the empirical attenuation coefficients could not account sufficiently for the scattering and beam hardening effects.

Application to a porous medium

Images of Flint sand packed into rectangular and cylindrical containers were used to check the empirical attenuation coefficients determined by fitting Eq. (4) to the calibration cell images. All of the porous media images were processed using the same steps as described for the calibration cells. Pore water thickness τ_{ij} (cm) was then calculated on a pixel by pixel basis (i,j) using Eq. (8).

To compute the volumetric water content (θ_{ij} , $\text{cm}^3 \text{ cm}^{-3}$) at a pixel(i,j) from neutron radiography of a rectangular container, the measured water thickness was divided by the beam path length (l_{ij}), ($=2.62$ cm), i.e.

$$\theta_{ij} = \frac{\tau_{ij}}{l_{ij}} \times \frac{\text{pixel area}}{\text{pixel area}} = \frac{\tau_{ij}}{l_{ij}}. \quad (9)$$

To compute the volumetric water content (θ_{ij}) from neutron radiography of a cylindrical container, the measured water thicknesses were corrected for variations in the transmission path length of neutrons based on the chord length (C_{ij}) for a circle (Eq. (4)).

The volumetric water content at the pixel(i,j), θ_{ij} ($\text{cm}^3 \text{ cm}^{-3}$) is then the ratio of the measured water thickness to the chord length

$$\theta_{ij} = \frac{\tau_{ij}}{C_{ij}} \times \frac{\text{pixel area}}{\text{pixel area}} = \frac{\tau_{ij}}{C_{ij}}. \quad (10)$$

In order to compare changes in total water volume obtained by neutron radiography with those obtained independently from the hanging water column method, the total water volume using neutron radiography was calculated from the average volumetric water content. To obtain the average volumetric water content ($\langle \theta_v \rangle$) for each suction applied, the individual θ_{ij} values from the neutron radiographs were arithmetically averaged over the

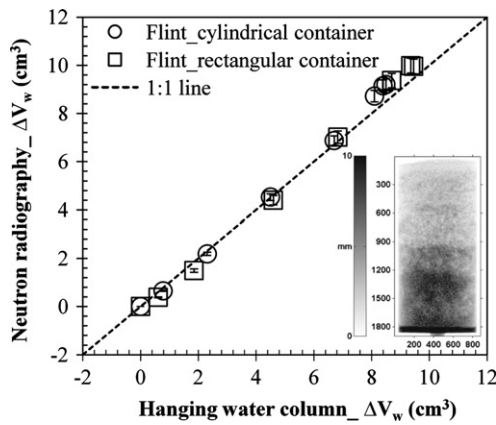


Fig. 11. Comparison of cumulative total water volume changes in Flint sand in rectangular (squares) and cylindrical (circles) containers measured by neutron radiography and the conventional hanging water column method at quasi-equilibrium during monotonic drying. The error bars represent the 95% confidence intervals (note: some of the confidence intervals are too small to be seen). Inset shows the water thickness distribution within the sample at $\Delta V_w = 4.5 \text{ cm}^3$ for the cylindrical sand column.

imaged area, i.e.

$$\langle \theta_v \rangle = \frac{\sum_{i=1}^n \theta_{ij}}{n} \quad (11)$$

where n is the total number of pixels in the ROI.

The expressions used to compute the total water volumes in the rectangular and cylindrical containers are given below

$$V_w(\text{cm}^3) = \langle \theta_v \rangle \times n \times l_{ij} \times \text{pixel area}$$

$$V_w(\text{cm}^3) = \langle \theta_v \rangle \times \sum_{i=1}^n (C_{ij} \times \text{pixel area}) \quad (12)$$

where V_w is total volume of water in the column, $\langle \theta_v \rangle$ is the average volumetric water content at a given suction, n is the total number of pixels in the ROI, l_{ij} is the beam path length for the rectangular container, and C_{ij} is the chord length for the cylindrical container. 95% confidence intervals were calculated by varying the ROI; four different ROIs were selected for these calculations.

The cumulative water volume changes were calculated by subtracting the water volume of the driest image during the drainage process. The cumulative water volume changes in the porous media determined by neutron radiography were compared with those recorded by direct reading from the burette connected to a hanging water column. Fig. 11 shows the results of cumulative average water volume changes in Flint sand measured in rectangular and cylindrical containers at quasi-equilibrium during monotonic drying. The changes in total water volumes measured in the rectangular and cylindrical containers were very similar showing no significant effect on the quantification in relation to sample geometry. Neutron radiography slightly overestimates the water volume changes relative to the results from the hanging water column, especially at high water volumes ($> \sim 8 \text{ cm}^3$) contrary to the water calibration data in Fig. 10. This contrast result might be due to summation of errors since we used cumulative changes in water volume for the porous medium. However, data from both the rectangular and cylindrical containers are generally in good agreement with the hanging water column measurements (i.e., close to the 1:1 line).

Conclusions

Data from each calibration cell type (rectangular and cylindrical) showed little variation in transmission for the same water

thickness. There was no significant effect due to geometry or cell designs for the water calibration experiments. Strong scattering effects were observed with increasing thickness of water ($> 0.2 \text{ cm}$) when the water calibration cells were positioned close to the face of the detector (0 and 2.4 cm away). Accurate quantification of volumetric water contents in calibration cells and porous media using neutron radiography data can be obtained with empirical attenuation coefficients for water determined at some distance from the detector (in this case, 24 cm). These coefficients were obtained by fitting Eq. (7) to experimental water calibration data from rectangular and cylindrical calibration cells by means of non-linear regression. The resulting estimates were successfully applied to quantify changes in the total water volume of packed columns of Flint sand. Changes in cumulative total water volumes determined by neutron radiography showed good agreement with those obtained by the conventional hanging water column method. These results allow extension of the calibration equation to the quantification of high water contents within other samples of porous media positioned at a specific distance from the detector. The parameters (Σ and β) presented in this paper are unique for HFIR CG-1D. Other facilities can determine unknown water contents by obtaining their own unique Σ and β parameters for water at an optimal sample location in a specific beam line. The optimal sample location can be found, depending on the maximum water content of the sample, for a specific detector at each beam line by examination of the measured neutron transmission for water calibration cells positioned at a few selected locations.

Acknowledgments

This research was supported by the Laboratory Directed Research and Development (LDRD) Program of Oak Ridge National Laboratory and the Joint Directed Research and Development (JDRD) Program of the University of Tennessee UT-ORNL Science Alliance. The authors are thankful for contributions from Lakeisha Walker, Keely Willis, and the HFIR support groups, especially the HFIR Machine Shop, Brent Taylor, Gary Lynn, Lisa Fagan, Jaimie Werner, and the Instrument Development Group. The detector set-up was developed in collaboration with Prof. Dayakar Penumadu in the Department of Civil and Environmental Engineering at the University of Tennessee-Knoxville. This research at Oak Ridge National Laboratory's High Flux Isotope Reactor was sponsored by the Scientific User Facilities Division, Office of Basic Energy Sciences, U.S. Department of Energy, which is managed by UT-Battelle, LLC.

References

- [1] M. Strobl, I. Manke, N. Kardjilov, A. Hilger, M. Dawson, J. Banhart, *Journal of Physics D: Applied Physics* 42 (2009) 243001.
- [2] I.S. Anderson, R. McGreevy, H. Bilheux, *Neutron Imaging and Applications: A Reference for the Imaging Community*, Springer, New York, 2009.
- [3] A. Bayer, H.-J. Vogel, K. Roth, *Hydrology and Earth System Sciences* 8 (2004) 2.
- [4] M.G. Basavaraj, G.S. Gupta, *Iron Steel Institute Japan (ISIJ Int.)* 44 (2004) 50.
- [5] S. Oswald, W. Kinzelbach, A. Greiner, G. Brix, *Geoderma* 80 (1997) 417.
- [6] L.D. Hall, G.M.H. Amin, E. Dougherty, M. Sanda, J. Votruba, K.S. Richards, R.J. Chorley, M. Cislserova, *Geoderma* 80 (1997) 431.
- [7] A. Turhan, K. Heller, J.S. Brenizer, M.M. Mench, *Journal of Power Sources* 160 (2006) 1195.
- [8] T.A. Trabold, J.P. Owejan, J.J. Gagliardo, D.L. Jacobson, D.S. Hussey, M. Arif, *Use of neutron imaging for proton exchange membrane fuel cell (PEMFC) performance analysis and design*, *Handbook of Fuel Cells—Fundamentals, Technology and Applications*, Wiley and Sons, 2009 (Chapter 44).
- [9] S.E. Oswald, M. Menon, A. Carminati, P. Vontobel, E. Lehmann, R. Schulin, *Vadose Zone Journal* 7 (2008) 1035.
- [10] A.B. Moradi, H.M. Conesa, B.H. Robinson, E. Lehmann, G. Kühne, A. Kaestner, R. Schulin, *Plant Soil* 318 (2009) 243.

- [11] V. Cnudde, M. Dierick, J. Vlassenbroeck, B. Masschaele, E. Lehmann, P. Jacobs, L. Van Hoorebeke, Nuclear Instruments and Methods in Physics Research Section B 266 (2008) 155.
- [12] L.G. Tumlinson, H. Liu, W.K. Silk, J.W. Hopmans, Soil Science Society of America Journal 72 (2008) 1234.
- [13] I. Hincapié, P. Germann, Vadose Zone Journal 8 (2009) 891.
- [14] I. Hincapié, P. Germann, Vadose Zone Journal 9 (2010) 278.
- [15] C.-L. Cheng, M. Kang, E. Perfect, S. Voisin, J. Horita, H.Z. Bilheux, J.M. Warren, D.L. Jacobson, D.S. Hussey, Soil Science Society of America Journal 76 (2012) 1164.
- [16] W. Treimer, M. Strobl, N. Kardjilov, A. Hilger, I. Manke, Applied Physics Letter 89 (2006) 203504.
- [17] N. Kardjilov, S. Baechler, M. Bastürk, M. Dierick, J. Jolie, E. Lehmann, T. Materna, B. Schillinger, P. Vontobel, Nuclear Instruments and Methods in Physics Research Section A 501 (2003) 536.
- [18] N. Kardjilov, B. Schillinger, E. Steichele, Applied Radiation and Isotopes 61 (2004) 455.
- [19] E.H. Lehmann, P. Vontobel, N. Kardjilov, Applied Radiation and Isotopes 61 (2004) 503.
- [20] R. Hassanein, E. Lehmann, P. Vontobel, Nuclear Instruments and Methods in Physics Research Section A 542 (2005) 353.
- [21] N. Kardjilov, F.C. De Beer, R. Hassanein, E. Lehmann, P. Vontobel, Nuclear Instruments and Methods in Physics Research Section A 542 (2005) 336.
- [22] D.S. Hussey, D.L. Jacobson, K.I. Coakley, D.F. Vecchia, M. Arif, Journal of Fuel Cell Science and Technology 7 (2010) 22.
- [23] F. Kim, D. Penumadu, D.S. Hussey, Journal of Geotechnical and Geoenvironmental Engineering 138 (2011) 147.
- [24] R. Hassanein, F. de Beer, N. Kardjilov, E. Lehmann, Physica B 385–386 (2006) 1194.
- [25] D.S. Hussey, D.L. Jacobson, Neutron radiography for PEMFCs: high resolution studies, in: C. Hartnig, C. Roth (Eds.), Polymer Electrolyte Membrane and Direct Methanol Fuel Cell Technology, vol. 2; in situ characterization of PEMFCs and DMFCs, Woodhead, Cambridge, UK, 2012.
- [26] A.S. Tremsin, W.B. Feller, R.G. Downing, Nuclear Instrument and Methods in Physics Research Section A 539 (2005) 278.
- [27] H. Bilheux, K. Crawford, L. Walker, S. Voisin, M. Kang, M. Harvey, B. Bailey, M. Phillips, J.-C. Bilheux, K. Berry, J. Ankner, J. Warren, J. Nanda, S. Pannala, M. Lance, Neutron imaging at the Oak Ridge National Laboratory: present and future capabilities, in: 7th International Topical Meeting on Neutron Radiography, in press.
- [28] M. Arif, D.L. Jacobson, D.S. Hussey, Neutron Imaging Study of the Water Transport in Operating Fuel Cells; DOE Hydrogen Program FY 2009 Annual Progress Report, <http://www.hydrogen.energy.gov/pdfs/progress09/v_a_8_arif.pdf>.
- [29] <<http://www.mathworks.com>>.
- [30] W.S. Rasband, ImageJ, USNational Institutes of Health, Bethesda, Maryland, USA, (1997–2008), <<http://rsb.info.nih.gov/ij/>>.
- [31] SAS/STAT 9.2 User's Guide: The NLIN Procedure Book Excerpt, 2008.